Nano Research

Open Access

Research Article

Se-doped MnO_2 as a low-cost and high-efficiency catalyst for acidic oxygen evolution reaction

Sanjiang Pan[1,2,3,§] ✉, Shenao Wang[1,§], Zishuo Xie[1], Hang Li[1], Yang Fu[4], and Desong Wang[2] ✉

[1] School of Vehicle and Energy, Yanshan University, Qinhuangdao 066004, China
[2] State Key Laboratory of Metastable Materials Science and Technology, Yanshan University, Qinhuangdao 066004, China
[3] Hebei Engineering Research Center for Low Carbon Development and Resource Utilization of Fossil Energy Sources, Yanshan University, Qinhuangdao 066004, China
[4] Jiangmen Laboratory of Carbon Science and Technology, Jiangmen 529020, China
[§] Sanjiang Pan and Shenao Wang contributed equally to this work.

Cite this article: *Nano Research*, **2025**, *18*, 94907912. https://doi.org/10.26599/NR.2025.94907912

ABSTRACT: Developing acid-stable manganese-based catalysts for the oxygen evolution reaction (OER) is pivotal for advancing proton exchange membrane water electrolysis (PEMWE). Here, we present a selenium-doped MnO_2 catalyst, where the synergistic effects of Se and oxygen defects stabilize Mn^{3+} species and regulate *OH adsorption dynamics. *In situ* spectroscopic studies and density functional theory (DFT) calculations confirm that Se doping modulates the electronic structure of Mn centers, lowering the energy barrier for *OH deprotonation and accelerating OER kinetics. In 0.5 M H_2SO_4, Se-MnO_2 achieves current densities of 10 and 100 mA·cm^{-2} with overpotentials of 345 ± 5 and 398 ± 5 mV, respectively, outperforming commercial RuO_2. Integrated into PEM electrolyzers, the catalyst demonstrates exceptional stability over 400 h under dynamic current densities (100–500 mA·cm^{-2}), showcasing structural integrity and negligible activity decay. The strategic doping of selenium significantly enhances catalytic performance, thereby offering a promising pathway toward the development of cost-effective electrocatalysts for applications under acidic conditions.

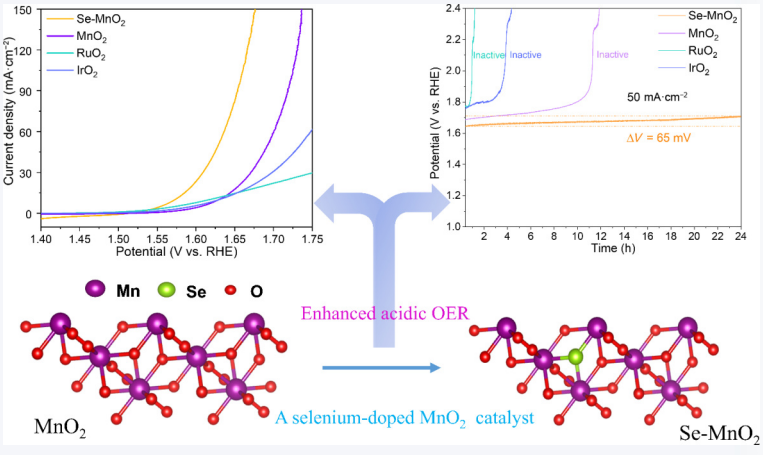

KEYWORDS: non-noble metal, proton exchange membrane, acid oxygen evolution reaction, manganese-based catalysts, hydrogen production

1 Introduction

Hydrogen production through renewable energy-powered water electrolysis has emerged as a pivotal strategy for achieving carbon neutrality, owing to its compatibility with intermittent energy sources and capacity for large-scale green hydrogen generation [1–4]. Proton exchange membrane water electrolysis (PEMWE), by virtue of its excellent power density, extremely low Ohmic loss, and rapid dynamic response capacity, emerges as a crucial leading technology promoting the development of the sustainable hydrogen economy [5, 6]. However, the sluggish kinetics and high energy barriers of the oxygen evolution reaction (OER)—a critical half-reaction involving four proton-coupled electron transfers—severely limit PEMWE efficiency, particularly under acidic conditions [7–9]. The corrosive, proton-rich environment exacerbates catalyst degradation, demanding electrocatalysts that balance exceptional activity with structural robustness [10].

Current state-of-the-art acidic OER catalysts predominantly rely on scarce precious metals like iridium and ruthenium oxides [11–15]. While IrO_2 demonstrates moderate stability, its prohibitive cost and limited natural abundance hinder widespread PEMWE

Received: May 10, 2025; **Revised:** July 26, 2025
Accepted: August 12, 2025

✉Address correspondence to Desong Wang, dswang06@126.com; Sanjiang Pan, pansanjiang@ysu.edu.cn

adoption. Ruthenium-based alternatives, though initially active, undergo catastrophic dissolution via over-oxidation to soluble RuO_4^- under operational potentials [16, 17]. Manganese oxides (MnO_x) have been studied extensively in the field of non-precious metals recently [18–21], inspired by their natural abundance and the stability of Mn^{3+} centers in biological oxygen-evolving complexes [22, 23]. However, MnO_x suffers from rapid deactivation in acidic media due to Mn^{3+} disproportionation and oxidative dissolution, necessitating innovative stabilization strategies [24–27]. Doping engineering has proven effective in modulating electronic structures to enhance catalytic durability [28–32]. The introduction of heteroatoms can optimize intermediate adsorption energetics while suppressing metal dissolution through charge redistribution and lattice strain effects [30–32]. Selenium, with its high electron density and metalloid characteristics, presents unique opportunities for stabilizing transition metal oxides. Theoretical studies suggest that Se incorporation could localize electron density at Mn active sites, strengthening metal–oxygen bonds and inhibiting over-oxidation [33, 34]. Nevertheless, achieving precise control over Se doping levels and understanding its dynamic role during OER remains challenging, hindering rational catalyst design.

Herein, we address these challenges through a defect engineering strategy that synergistically incorporates selenium dopants and oxygen defects into MnO_2 (Se-MnO_2). *In situ* electrochemical Raman spectroscopy and density functional theory (DFT) calculations reveal that Se doping preferentially stabilizes Mn^{3+} active centers while oxygen defects optimize *OH adsorption kinetics. This dual modification redirects the OER pathway toward a more energetically favorable mechanism, achieving a low overpotential of 345 ± 5 mV at 10 mA·cm^{-2} in 0.5 M H_2SO_4. When integrated into PEM electrolyzers, Se-MnO_2 demonstrates unprecedented stability over 400 h under dynamic current densities (100–500 mA·cm^{-2}), outperforming commercial RuO_2 benchmarks. Our work establishes a novel paradigm for designing acid-stable OER catalysts through targeted electronic structure modulation, accelerating the development of cost-effective PEMWE systems for green hydrogen production.

2 Experimental section

2.1 Synthesis of Se-MnO_2 catalyst

At the beginning of the experiment, 10 mL of a 4 M $Mn(NO_3)_2{\cdot}4H_2O$ solution was prepared. Precisely 0.1 mmol of SeO_2 was weighed and initially dissolved in 300 μL of anhydrous ethanol, followed by ultrasonic treatment for a defined duration. Subsequently, the solution was thoroughly mixed with 500 μL of the 4 M $Mn(NO_3)_2{\cdot}4H_2O$ solution and subjected to additional ultrasonic treatment for 20 min. The resulting mixture was then deposited onto carbon cloth (2 cm × 1.5 cm) via a thermal deposition method. A total of 200 μL of the solution was evenly applied in three aliquots onto the carbon cloth surface. After application, the samples were heated on a hot plate at 330 °C for 2 h, then cooled naturally to room temperature. Electrochemical measurements and *in-situ* Raman spectroscopy were subsequently performed. Prior to sample deposition, the carbon cloth was subjected to ultrasonic pretreatment to ensure uniform dispersion. For comparison, MnO_2 and other catalysts were prepared using a similar procedure but with varying metal precursor ratios.

2.2 Characterizations

X-ray diffraction (XRD) measurement was performed using Bruker D8 (Cu Kα radiation at 2 °·min^{-1}). Fourier transform infrared (FT-IR) spectroscopy and Raman spectroscopy were presented by Bruker's Vertex 70 and Xplora PLUS (HORIBA), respectively. The microstructure was characterized by transmission electron microscopy (TEM) and high-resolution TEM (HRTEM) measurements, and the crystal structure was identified by selected area electron diffraction (SAED, JEOL JEM-2800).

An X-ray photoelectron spectrometer (XPS, Thermo Fisher Scientific K-Alpha) was utilized for the analysis. The analytical chamber maintained a vacuum level of 5 × 10^{-10} Pa. For excitation, Al Kα radiation ($h\nu$ = 1486.68 eV) was employed, with an operating voltage set at 15 kV and a filament current of 10 mA. Signal accumulation was performed over 5 to 10 cycles. The pass energy during testing was 30 eV, with a step size of 0.05 eV. The C 1s peak at 284.80 eV was used as the energy reference standard.

2.3 Electrochemical measurements

Electrochemical experiments were carried out using a CHI-660E electrochemical workstation (CH Instruments Inc., China) in a three-electrode configuration at 25 °C within a 0.5 M H_2SO_4 solution. In these setups, a graphite rod and an Ag/AgCl electrode served as the counter electrode and reference electrode, respectively.

To prepare the RuO_2-loaded electrode, 60 mg of RuO_2 was dispersed in 8 mL of isopropanol, followed by thorough mixing and ultrasonic treatment. Subsequently, 12 mg of carbon black was added, mixed uniformly, and subjected to further ultrasonic processing. A 120 μL aliquot of naphthol solution was then incorporated to finalize the electrode preparation. For the carbon paper electrode (dimensions: 2 cm × 1.5 cm), identical processing steps were applied as those used for the carbon cloth. The resulting solution was coated onto the carbon paper and dried at 60 °C for 3 h. To prepare the IrO_2-loaded electrode, 15 mg of IrO_2 was dispersed in 1 mL of ethanol, followed by thorough mixing and ultrasonic treatment. A 15 μL aliquot of naphthol solution was then incorporated to finalize the electrode preparation. For the carbon cloth electrode (dimensions: 0.5 cm × 1.5 cm), the resulting solution was coated onto the carbon cloth and dried at 60 °C for 3 h.

Prior to conducting linear sweep voltammetry (LSV) measurements, cyclic voltammetry (CV)-based electrochemical activation was performed at a scan rate of 50 mV·s^{-1} until the electrodes reached stability. LSV tests were subsequently carried out at scan rates of 5 and 1 mV·s^{-1}. The reversible hydrogen electrode (RHE) potential (E) was derived from the Ag/AgCl reference using the Nernst equation

$$E(\mathrm{RHE}) = E(\mathrm{Ag/AgCl}) + 0.197\ \mathrm{V} + 0.059 \times \mathrm{pH} \quad (1)$$

Electrochemical impedance spectroscopy (EIS) was utilized to assess the performance of the catalyst samples. For comparative purposes, EIS spectra were recorded over a frequency range of 0.01 Hz to 100 kHz. Series resistance (R_s) values obtained from EIS experiments were employed to correct polarization data and facilitate subsequent Tafel analysis

$$E_{\mathrm{corrected}} = E - iR \quad (2)$$

where $E_{\mathrm{corrected}}$ is obtained by measuring the voltage and then subtracting the product of the current and the uncompensated ohmic resistance. R is the uncompensated Ohmic resistance.

Double-layer capacitance (C_{dl}) was obtained by collecting CVs at various scan rates of 4, 6, 8, 10, and 12 mV·s^{-1}. Effective

electrochemical surface area (ECSA) was obtained from the C_{dl} value

$$\mathrm{ECSA} = \frac{C_{dl}}{C_s} \times S \tag{3}$$

where S is the electrode geometrical area. C_s is the specific capacitance of the sample, and a typical value of 0.035 mF·cm^{-2} as reported was used in this work.

The specific or observed reaction rate constant (K) or maximum velocity was measured at various temperatures (30 to 45 °C), and the activation energy (E_a (J·mol^{-1})) of the catalyst sample was determined experimentally using the Arrhenius equation (Segel, 1993). The log$K$ values were plotted against $1/T$ (Arrhenius plot), and the E_a was derived from the slope of the linear portion of this plot. log$K$ is calculated, and the E_a of the prepared catalyst sample is experimentally determined

$$\mathrm{Slope} = \frac{-E_a}{2.303 \times R \times T} = \frac{\lg K_2 - \lg K_1}{\left(\frac{1}{T_2} - \frac{1}{T_1}\right) \times 10^{-3}} \tag{4}$$

where R is gas constant (8.314 J·mol^{-1}·K^{-1}) and T is absolute temperature (K). T_1 and T_2 are the measured Kelvin temperatures, while K_1 and K_2 are the reaction rate constants calculated at their corresponding temperatures.

The theoretical volume ($V_{theoretical}$) of the released gas was calculated using the equation

$$\eta = \frac{V_{experimental}}{V_{theoretical}} \times 100\% \tag{5}$$

$$V_{theoretical} = \frac{I \times t \times V_m}{n \times \mathrm{F}} \tag{6}$$

where η refers to Faraday efficiency, which is the ratio of the experimentally released gas volume to the theoretically released gas volume. $V_{experimental}$ represents the experimental volume, I represents the experimental current, t is the recorded time, V_m is the molar volume of 1 mol O_2, n is the number of electrons required for 1 mol O_2, and F is the Faraday constant (96,485 C·mol^{-1}).

2.4 DFT calculations

All first-principles calculations were conducted using spin-polarized DFT, implemented via the Vienna *ab initio* simulation package (VASP), which was powered by cp2k_2023.1. To model the interaction between ions and electrons, the projector augmented wave (PAW) method was employed, while the electron exchange-correlation interaction was described using the generalized gradient approximation (GGA) based on the Perdew–Burke–Ernzerhof (PBE) functional. Additionally, DFT + U (U is the electrode potential) corrections were incorporated into the electronic structure calculations. The kinetic energy cutoff was set to 400 eV, with an energy convergence threshold of 1×10^{-4} eV and a force convergence limit of −0.05 eV. A k-point mesh of 3 × 3 × 1 centered at the gamma point was utilized for sampling in the Brillouin zone. All systems included a vacuum layer of approximately 15 Å to prevent interactions between neighboring cells.

Following the methodology proposed by Norskov et al., the change in free energy (ΔG) from the initial to the final state for each OER elementary step was defined as

$$\Delta G = \Delta E_1 + \Delta E_{ZPE} - T\Delta S + \Delta G_U + \Delta G_{pH} \tag{7}$$

where ΔE_1 is the calculated total energy; ΔE_{ZPE} is the zero-point energy; ΔS is the entropy difference between reactants and products; T = 298.15 K; $\Delta G_U = -neU$, where e is the charge transferred, and n is the number of transferred electrons; and $\Delta G_{pH} = -K_B T \ln[\mathrm{H}] = \mathrm{pH} \times K_B^+ T \ln 10$, where K_B is the Boltzmann constant.

Consequently, the free energy changes for the four elementary processes are denoted as follows: $\Delta G_1 = \Delta G_{OH^*} - \Delta G_*$, $\Delta G_2 = \Delta G_{O^*} - \Delta G_{OH^*}$, $\Delta G_3 = \Delta G_{OOH^*} - \Delta G_{O^*}$, and $\Delta G_4 = \Delta G_* - \Delta G_{OOH^*}$. ΔG_1, ΔG_2, ΔG_3, and ΔG_4 are the free energy changes for the four elementary processes. ΔG_{OH^*}, ΔG_*, ΔG_{O^*}, and ΔG_{OOH^*} correspond to their free energy in the OH*, *, O*, and OOH* states respectively. Furthermore, the overpotential of OER performance (η_{OER}) can be assessed using Eq. (8)

$$\eta_{OER} = \frac{\max(\Delta G_1, \Delta G_2, \Delta G_3, \Delta G_4)}{e} - 1.23 \tag{8}$$

This approach allowed for a comprehensive evaluation of the OER mechanism and its associated energetics.

3 Results and discussion

3.1 Materials characterization

The crystal structure of Se-MnO_2 was characterized by XRD characterization method. The XRD results of the prepared Se-MnO_2 samples exhibited characteristic peaks that precisely corresponded to the standard pattern of MnO_2 (PDF #44-0141) (Fig. 1(a)), indicating that Se-MnO_2 possesses a complete and favorable prototype crystal structure of MnO_2, and no characteristic peaks belonging to SeO_2 or other impurity peaks were observed. Additionally, the Raman spectra of MnO_2 revealed four distinct Raman peaks at 385, 499, 571, and 647 cm^{-1}, corresponding to the A_{1g}, E_g, A_{1g}, and A_{2g} vibration modes, respectively (Fig. 1(b)). Through comparison, it was found that the Raman characteristic peaks of Se-MnO_2 almost completely corresponded to those of MnO_2, while they significantly differed from those of SeO_2. Simultaneously, the locally magnified Raman spectra indicate that the Raman characteristic peaks of Se-MnO_2 shifted by ~ 4 cm^{-1} in the redshift direction compared to MnO_2 (Fig. S1 in the Electronic Supplementary Material (ESM)), suggesting that the Se element was successfully doped into the lattice structure of MnO_2, which was consistent with the XRD results. In the SAED pattern of the Se-MnO_2 samples, distinct diffraction rings attributed to the MnO_2 crystal planes (521), (440), (301), (221), and (220) were observed (Fig. 1(c)), further demonstrating that the main crystal structure of MnO_2 was not influenced by Se doping.

In the locally magnified high-angle annular dark-field scanning TEM (HAADF-STEM) image of the Se-MnO_2 sample, lattice fringes with lattice spacings of 0.154 and 0.236 nm and an angle of 82° can still be clearly observed, corresponding to the (521) and (211) crystal planes of MnO_2, respectively (Fig. 1(e)). More importantly, a large number of atomically dispersed bright spots (marked with yellow circles) of Se atoms are clearly visible and uniformly distributed on the surface of Se-MnO_2, confirming that during the ion exchange process, Se elements are anchored on MnO_2 in the form of single atoms (Fig. 1(d)). The energy-dispersive X-ray spectroscopy (EDX) mapping of the Se-MnO_2 sample reveals

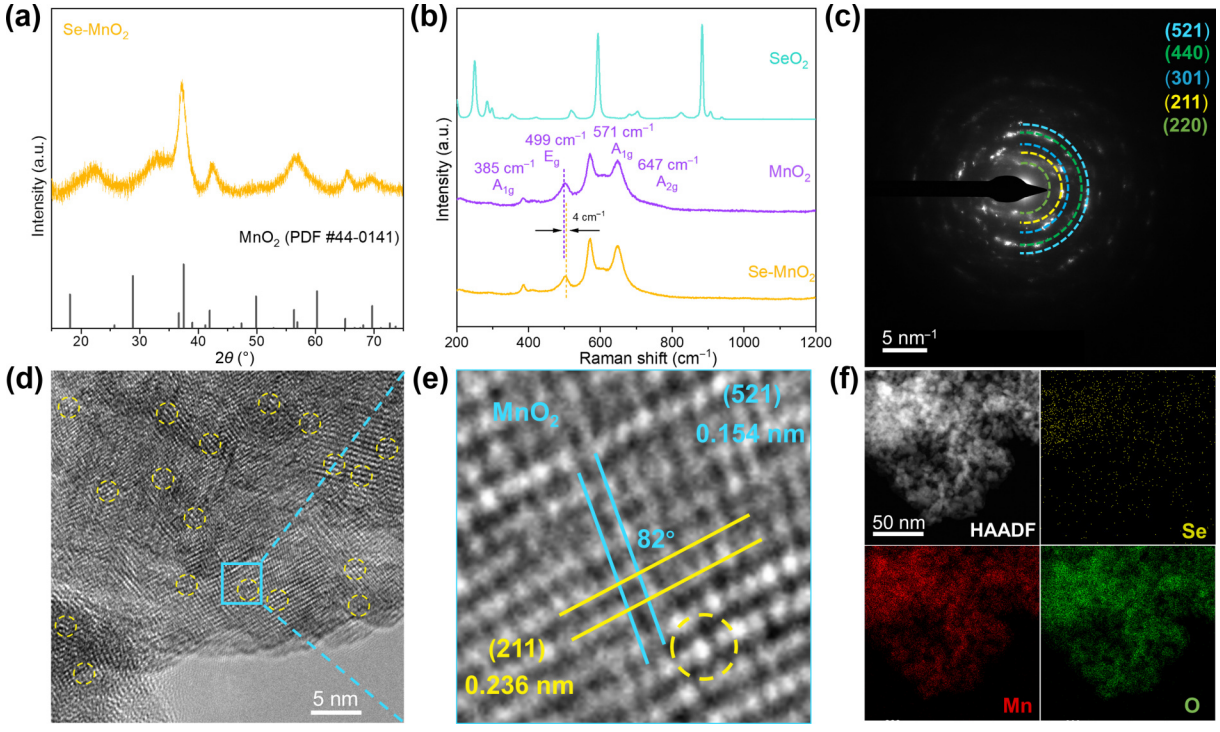

Figure 1 (a) XRD pattern of Se-MnO_2. (b) Raman spectra of Se-MnO_2, MnO_2, and SeO_2 in air. (c) SAED pattern of Se-MnO_2. (d) and (e) HRTEM images of Se-MnO_2. (f) HAADF-STEM and the corresponding elemental mappings of Se, Mn, and O in the images of Se-MnO_2.

that the elements O, Mn, and Se are uniformly distributed over the entire surface of the material, and the elements Mn and Se are interlaced (Fig. 1(f)). Elemental analysis reveals that the content of Se element is relatively lower compared to that of Mn and O elements (Fig. S2 and Table S1 in the ESM), thereby indicating the successful preparation of MnO_2 catalysts doped with a small amount of Se.

3.2 Evaluation of electrochemical activity

To validate the enhancement effect of selenium doping in Se-MnO_2 on the activity of the acidic OER, we selected MnO_2 as the baseline catalyst and made a comparison with the noble metal catalysts RuO_2 and IrO_2. LSV tests were carried out at a scan rate of 1 mV·s^{-1} in 0.5 M H_2SO_4 electrolyte (Fig. 2(a)). After *iR* correction, Se-MnO_2 exhibited a lower electrocatalytic overpotential, merely demanding 345 ± 5 mV when reaching a current density of 10 mA·cm^{-2}, which was significantly lower than that of MnO_2 (400 ± 5 mV), RuO_2 (386 ± 5 mV), and IrO_2 (400 ± 5 mV). At a higher current density of 50 mA·cm^{-2}, the overpotential of Se-MnO_2 was 398 ± 5 mV, markedly lower than that of MnO_2 (463 ± 5 mV), RuO_2 (613 ± 5 mV), and IrO_2 (505 ± 5 mV) (Fig. S3 in the ESM). Moreover, the Tafel slope of Se-MnO_2 was merely 64.5 mV·dec^{-1}, lower than that of MnO_2 (79.6 mV·dec^{-1}), RuO_2 (164.1 mV·dec^{-1}) and IrO_2 (121.6 mV·dec^{-1}), indicating a faster kinetic rate (Fig. 2(b)). The overpotential parameters and corresponding Tafel slopes of non-noble metal-based catalysts under acidic conditions at a current density of 10 mA·cm^{-2} were collated (Fig. 2(c)), and the detailed information of the aforementioned catalysts is listed in Table S3 in the ESM. The results suggest that the performance of Se-MnO_2 is superior to that of the majority of the reported non-noble metal-based catalysts. EIS indicated that the charge transfer resistance (R_{ct}) in the low-frequency region of Se-MnO_2 was 19.36 Ω, significantly lower than that of MnO_2 (100.1 Ω), RuO_2 (24.97 Ω), and IrO_2 (40.55 Ω) (Fig. 2(d)), demonstrating that the incorporation of selenium can effectively enhance the electron transfer ability of MnO_2. The intrinsic catalytic activity of various catalysts can be obtained by testing the ECSA (Figs. S4–S7 in the ESM), and the C_{dl} can be derived by further processing the ECSA data (Fig. 2(e)). The C_{dl} value of the Se-MnO_2 sample is 289.4 mF·cm^{-2}, which is lower than that of MnO_2 (568.3 mF·cm^{-2}) but higher than that of RuO_2 (23.9 mF·cm^{-2}) and IrO_2 (24.1 mF·cm^{-2}), suggesting that the Se-MnO_2 catalyst can achieve more excellent performance with a smaller active area compared to the MnO_2 catalyst. The ECSA values for each material were determined as follows: Se-MnO_2 (4134.3 cm^2), MnO_2 (8118.5 cm^2), RuO_2 (341.4 cm^2), and IrO_2 (343.4 cm^2). Subsequent ECSA correction of the LSV curves conclusively demonstrated the comparatively superior intrinsic activity of Se-MnO_2 compared to the MnO_2 (Fig. S8 in the ESM). Additionally, the E_a of the catalysts was calculated through the LSV curves tested at different temperatures (30, 35, 40, and 45 °C) (Figs. S9 and S10 in the ESM), and the results reveal that the E_a of Se-MnO_2 is 7.65 kJ·mol^{-1}, which is lower than that of MnO_2 (16.76 kJ·mol^{-1}) (Fig. 2(f)), indicating that the Se-MnO_2 catalyst is more prone to transform from the normal state to the active state.

A long-term stability test was performed at a current density of 50 mA·cm^{-2} using a three-electrode system (Fig. 2(g)). The results demonstrate that the MnO_2, RuO_2, and IrO_2 catalysts become completely deactivated after approximately 12, 2, and 4 h, respectively, while the decay rate of the Se-MnO_2 catalyst is 2.71 mV·h^{-1}, and it still retains excellent catalytic performance after 24 h. To further evaluate the durability of the Se-MnO_2 sample under simulated industrial conditions, the stability of the catalyst was tested in a PEMWE at 65 °C (Fig. 2(h)). During an extended 440 h durability test, the material demonstrated exceptional voltage retention characteristics: The average voltage decay rate remained at 0.227 mV·h^{-1} at 100 mA·cm^{-2}, showed negligible degradation at

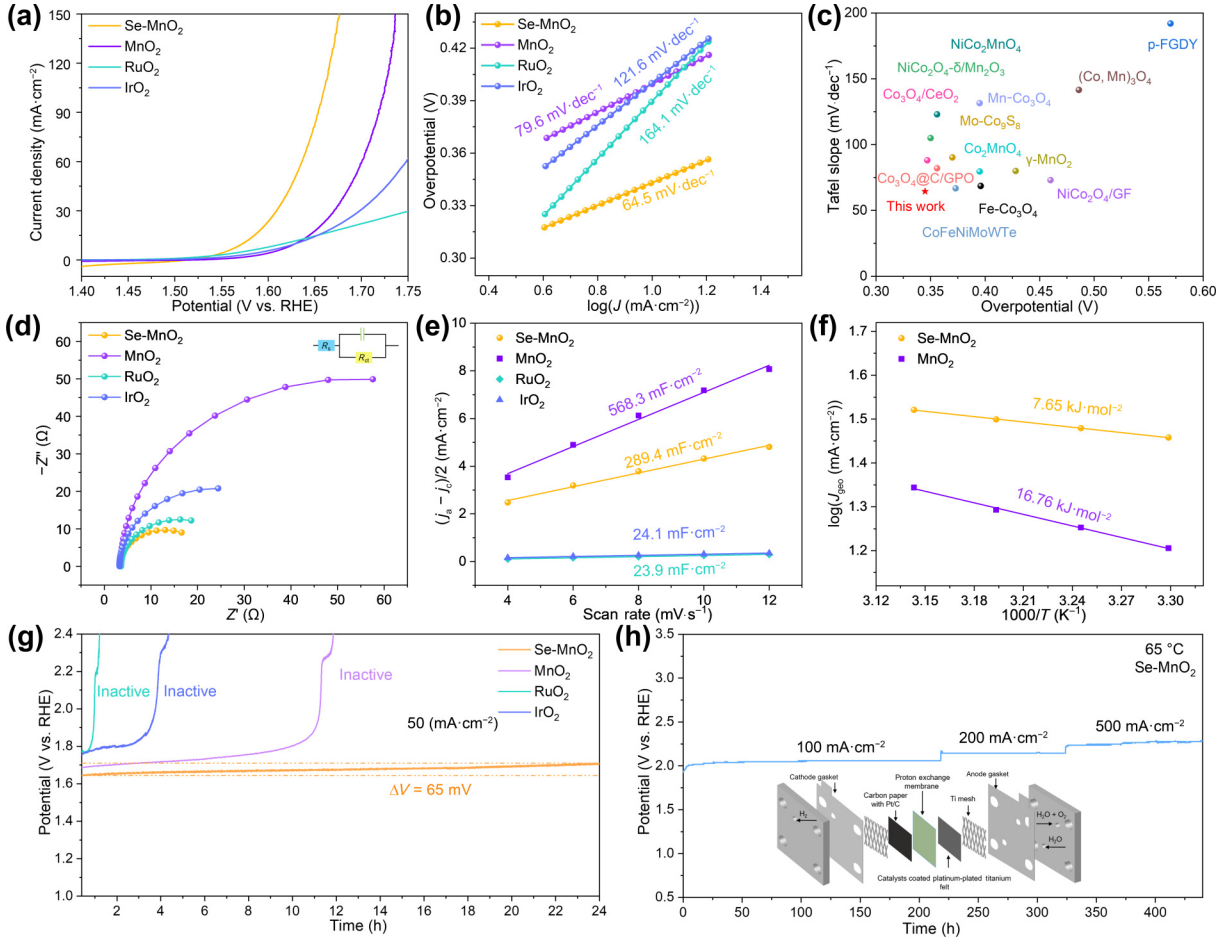

Figure 2 (a) OER polarization curves of Se-MnO_2, MnO_2, RuO_2, and IrO_2 at 1 mV·s^{-1} scan rate and negative scan after *iR* correction. (b) The corresponding Tafel slopes. (c) The Tafel slope and overpotential of OER with a current density of 10 mA·cm^{-2} were compared under acidic conditions with different electrocatalysts. (d) EIS Nyquist plots of Se-MnO_2, MnO_2, RuO_2, and IrO_2 at 1.33 V (set potential). The inset depicts the schematic diagram of the equivalent circuit. (e) Fitting plots show the C_{dl} values for Se-MnO_2 and MnO_2. (f) Arrhenius plots of OER specific activities of different catalysts at 1.63 V. (g) Chronopotentiograms of Se-MnO_2, MnO_2, RuO_2, and IrO_2 at 50 mA·cm^{-2}. (h) Chronopotentiometry tests of the Se-MnO_2 at 100, 200, and 500 mA·cm^{-2} in the PEM electrolyzer measured at 65 °C. Inset shows a photograph of the PEMWE.

200 mA·cm^{-2}, and maintained a controlled decay rate of 0.318 mV·h^{-1} even under ultrahigh current density of 500 mA·cm^{-2} (Table S3 in the ESM). These metrics surpass those of previously reported non-precious metal benchmark catalysts. Notably, a 150 min chronoamperometric test at 50 mA·cm^{-2} revealed a remarkable Faradaic efficiency of 99.47% (Fig. S11 and Table S2 in the ESM), confirming near-ideal charge transfer kinetics within the catalytic system. Comparative XRD analysis of the Se-MnO_2 catalyst before and after stability testing confirms retention of its crystalline phase structure, verifying the material's structural integrity (Fig. S12 in the ESM). These results indicate that doping Se into MnO_2 can prominently enhance its stability and catalytic performance.

3.3 X-ray photoelectron spectroscopy and *in situ* Raman analyses for mechanistic investigation

From the XPS spectrum analysis, it is known that in the full spectra of Se-MnO_2 and MnO_2 (Fig. 3(a)), the characteristic peaks of Mn, O, and C elements are prominent. In the Se-MnO_2 sample, the characteristic peak of the Se element is clearly visible, indicating the successful doping of Se into the MnO_2 structure (Fig. S13 in the ESM). To further investigate the influence of Se doping on the electronic structure of the active centers of the catalyst, we conducted a detailed analysis of the high-resolution XPS spectra of Mn 3s, O 1s, and Se 3d of Se-MnO_2 and MnO_2 catalysts (Figs. 3(b)–3(f)). As shown in Fig. 3(b) and Table S4 in the ESM, the Mn 3s binding energy spacings (ΔE) of Se-MnO_2 and MnO_2 are 5.16 and 4.70 eV, respectively. Among them, the ΔE value of 5.16 eV in Se-MnO_2 corresponds to the valence state of Mn^{3+}; while the ΔE value of 4.70 eV in MnO_2 is consistent with the standard value of Mn^{4+} reported in Ref. [35], confirming the successful synthesis of MnO_2. The valence state of manganese changes from +4 to +3, and Mn^{3+} is regarded as the highly active valence state for the OER reaction [25, 36]. Figure 3(e) presents the change in the Mn 3s ΔE of the Se-MnO_2 catalyst before and after the OER reaction. Before the OER, the ΔE value of Se-MnO_2 is 5.16 eV, corresponding to Mn^{3+}; after the OER, the ΔE value slightly increases to 5.19 eV, without any other significant changes, indicating that Se doping effectively inhibits the peroxidation-induced deactivation of Mn sites.

Additionally, through the analysis of the high-resolution O 1s XPS spectra, the distribution characteristics of different oxygen species in MnO_2 were studied. The characteristic peaks at 530.06 eV correspond to lattice oxygen ($O_{Lattice}$) (Fig. 3(c)). After Se doping,

the proportion of hydroxyl oxygen (O_{OH}) increases from 16.48% to 47.09%, while the proportion of $O_{Lattice}$ decreases from 83.52% to 52.91%. The presence of O_{OH} causes the delocalization of surface electrons, activating the catalyst surface and thereby enhancing the catalytic activity. The Se doping leads to an increase in the proportion of O_{OH} and a decrease in the proportion of $O_{Lattice}$, enhancing the surface activity of the catalyst. Figure 3(e) shows the changes in the O 1s spectra of the Se-MnO_2 catalyst before and after the OER reaction. After the OER, the O_{OH} content increases from 47.09% to 54.66%, while the $O_{Lattice}$ content decreases from 52.91% to 45.32%, but the overall change is not significant, indicating that the internal structure of the Se-MnO_2 catalyst maintains good stability. The high-resolution XPS spectra of the Se 3d orbital show the characteristic peaks at 53.78 and 54.58 eV, corresponding to Se $3d_{5/2}$ and Se $3d_{3/2}$, respectively (Fig. 3(f)). The position of Se $3d_{5/2}$ shifted to the right by 0.21 eV before and after the OER reaction of the Se-MnO_2 catalyst, indicating the direction of electron transfer in the Se-MnO_2 structure.

To achieve a more profound comprehension of the underlying mechanisms of the catalytic OER, we employed *in situ* Raman spectroscopy to investigate the active interface phase of the Se-MnO_2 catalyst during the electrochemical process. In a 0.5 M H_2SO_4 solution, *in situ* Raman experiments were conducted on the catalyst within the voltage range of 1.1 to 1.5 V to uncover its underlying mechanisms (Figs. S14–S16 in the ESM). Se-MnO_2 and MnO_2 catalysts presented seven peaks around 480, 515, 572, 609,

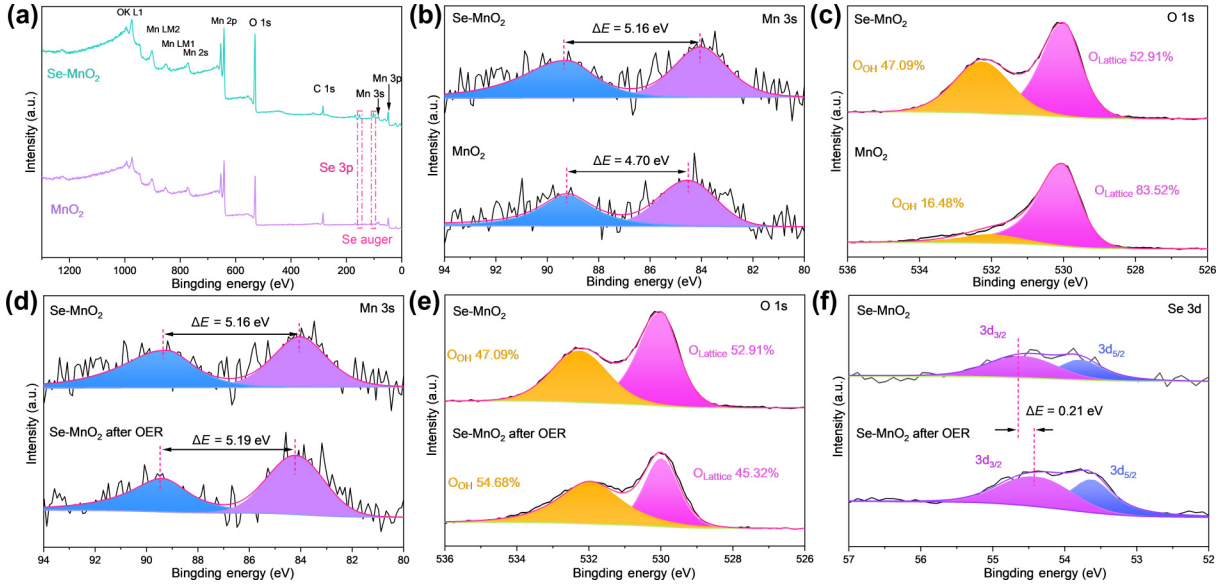

Figure 3 (a) Survey XPS spectra of Se-MnO_2 and MnO_2. ((b) and (c)) High-resolution (b) Mn 3s and (c) O 1s XPS spectra of Se-MnO_2 and MnO_2. ((d) and (e)) High-resolution (d) Mn 3s and (e) O 1s XPS spectra of Se-MnO_2 and Se-MnO_2 after OER. (f) High-resolution Se 4d XPS spectra of Se-MnO_2 and Se-MnO_2 after OER.

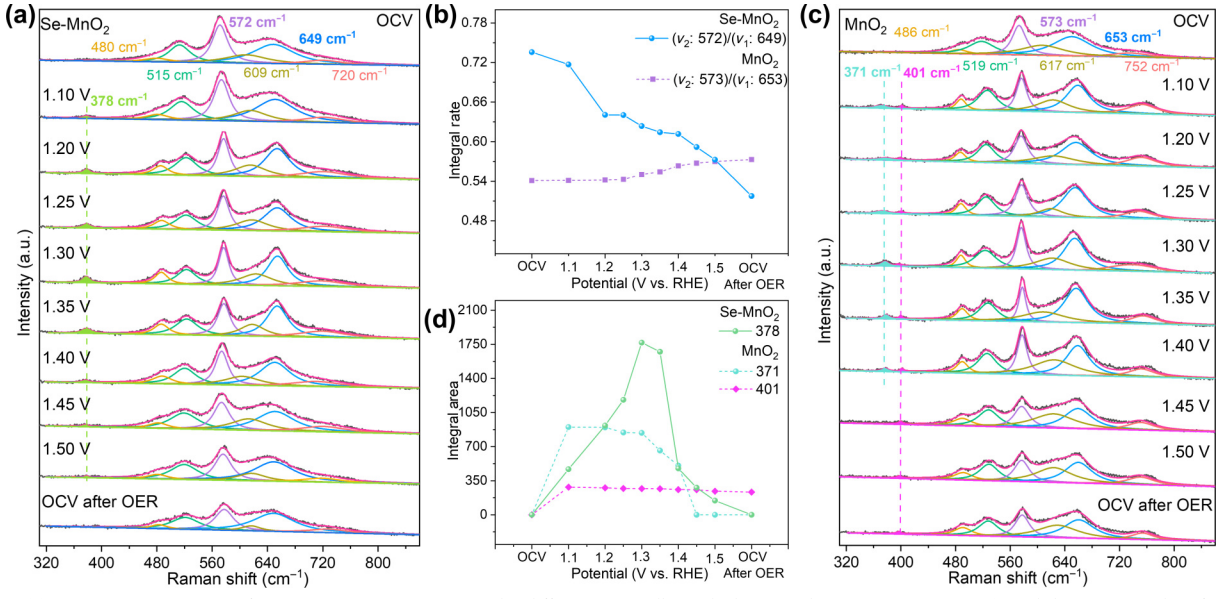

Figure 4 (a) *In situ* Raman spectra of Se-MnO_2 in 0.5 M H_2SO_4 under different externally applied potential (1.10–1.50 V vs. RHE), and the corresponding fitting line changes. (b) The location of bands ν_1 and ν_2 (the peak labeled ν_1 corresponds to the characteristic absorption at approximately 572 cm^{-1} and the peak labeled ν_2 corresponds to the characteristic absorption at approximately 649 cm^{-1}). The ratio of $I'(\nu_2)/I'(\nu_1)$ varies with the Se-MnO_2 potential, where I' represents spectral intensity. (c) *In situ* Raman spectra of MnO_2 in 0.5 M H_2SO_4 under different externally applied potentials (1.10–1.50 V vs. RHE) and the corresponding fitting line changes. (d) The evolution of characteristic peaks at 378 cm^{-1} versus the potential of Se-MnO_2. The evolution of characteristic peaks at 371 and 401 cm^{-1} versus the potential of MnO_2.

649, and 720 cm^{-1}, respectively, corresponding to the E_g, E_g, A_{1g}, A_g, A_{1g}, and B_{2g} vibrational modes in MnO_2 (Figs. 4(a) and 4(c)). Among them, the ratio of the peaks at 572 and 649 cm^{-1} exhibited a positive correlation with the interlayer spacing of the MnO_2 lattice [37, 38]. For the Se-MnO_2 catalyst, the ratio of the peaks at 572 and 649 cm^{-1} decreased with the increase in voltage, suggesting that during the OER reaction, the Se element of the Se-MnO_2 catalyst partially dissolved, leading to a reduction in the lattice spacing (Fig. 4(b)). In contrast, the ratio of the peaks at 573 and 653 cm^{-1} of the MnO_2 catalyst remained essentially unchanged. The dissolution of part of the Se element during the OER process is conducive to the formation of oxygen defects at the material interface and the optimization of the electronic structure, thereby enhancing the catalytic activity. This conclusion is consistent with the XPS results. Further analysis of the *in situ* Raman spectra of the Se-MnO_2 catalyst reveals that a new peak at 378 cm^{-1} emerged when the voltage was raised from 1.1 to 1.5 V and vanished at the open circuit voltage (OCV) (Fig. S15 in the ESM), which might be attributed to the formation of the Mn–OOH active species during the OER process. This favorable intermediate species adsorption can significantly boost the catalyst activity. Nevertheless, the *in situ* Raman spectra of the MnO_2 catalyst reveal that although the favorable adsorption of the key active species Mn–OOH at 371 cm^{-1} exists during the OER reaction process, an additional new peak (401 cm^{-1}) emerges as well (Fig. 4(d) and Fig. S17 in the ESM). This is the characteristic peak of α-MnO_2, suggesting that the MnO_2 catalyst undergoes an unfavorable phase transition during the OER reaction, resulting in additional energy loss and thereby manifesting poor OER activity.

To gain deeper insights into the OER mechanisms of MnO_2 and Se-doped MnO_2 catalysts, DFT calculations were performed. The dominant (211) crystal facets of MnO_2 and Se-MnO_2 were selected as models to simulate the OER pathways (Figs. 5(a) and 5(b)). The Gibbs free energy diagrams illustrate the free energy changes for each elementary reaction (Fig. 5(c)). The results show that the rate-determining step (RDS) for MnO_2 is OH* → O* with an energy barrier of 3.91 eV, while for Se-MnO_2, the RDS is * → OH* with a significantly reduced energy barrier of 1.46 eV. This indicates that

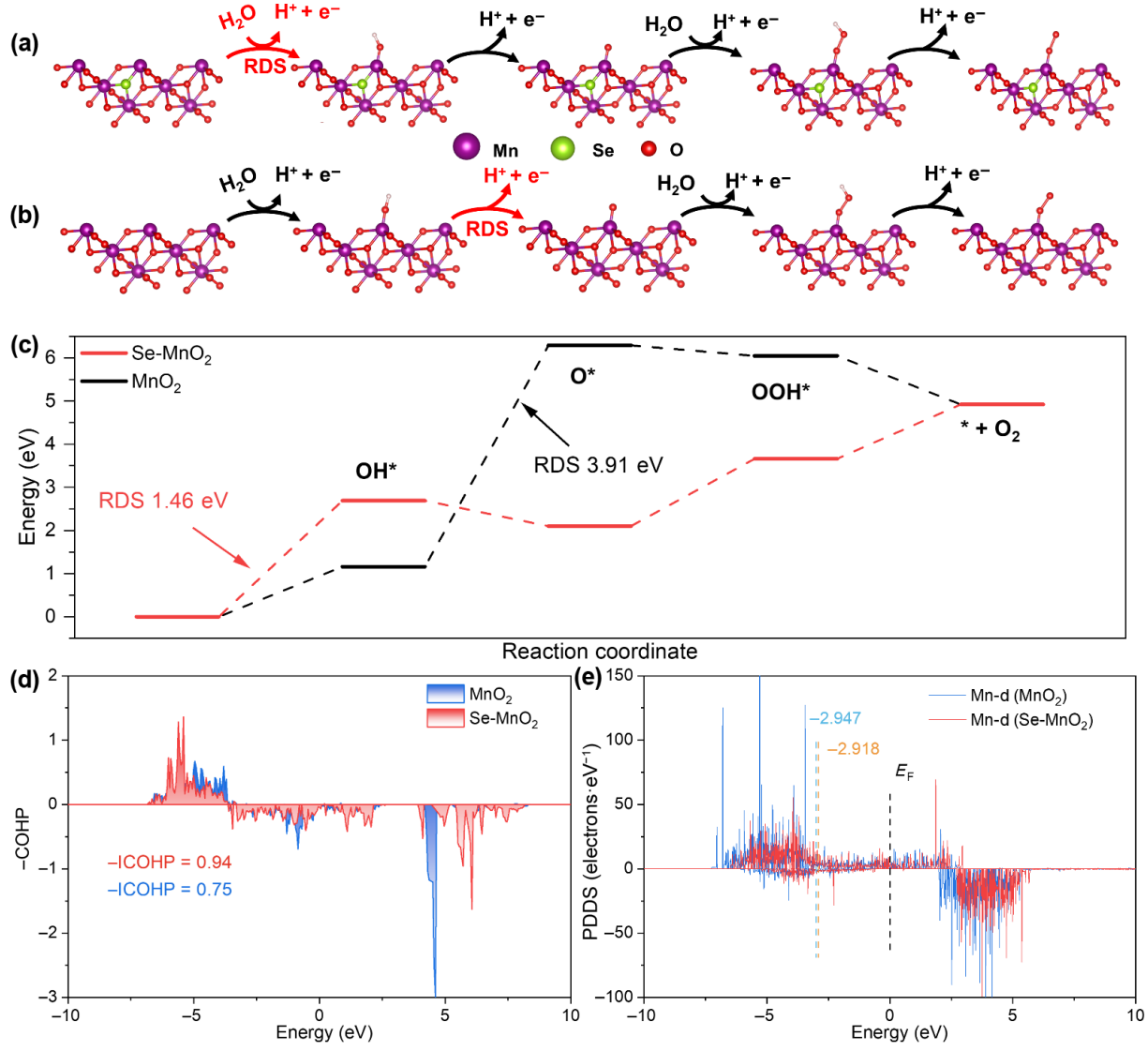

Figure 5 ((a) and (b)) Schematic illustration of the OER pathways, each reaction intermediate, and the corresponding RDS (marked in red) on the (a) Se-MnO_2 and (b) MnO_2 interface. (c) The Gibbs free energy diagrams for the OER pathway of Se-MnO_2 and MnO_2. (d) Calculated ICOHP values and schematic illustration of the oxygen-intermediates adsorption strength for Se-MnO_2 and MnO_2. (e) Projected density of state (pDOS) plots of Se-MnO_2 and MnO_2.

Se doping effectively lowers the E_a, consistent with electrochemical measurements. A lower E_a corresponds to faster reaction kinetics. Crystal orbital Hamiltonian population (COHP) analysis was conducted on the Mn–O bonds between active Mn sites and adsorbed O atoms. The bonding region below the Fermi level (E_F) was integrated, and the −integrated COHP (−ICOHP) value reflects bonding strength, with larger values indicating stronger interactions. The −ICOHP value for Se-MnO_2 (0.94) exceeds that of MnO_2 (0.75) (Fig. 5(d)), demonstrating that Se doping enhances the Mn–O bonding strength. Additionally, the projected Mn-d orbital density of states (Fig. 5(e)) reveals that the d-band center of Se-MnO_2 (−2.918 eV) is closer to E_F = 0 compared to MnO_2 (−2.947 eV). This shift suggests stronger adsorption of oxygen-containing intermediates on Se-MnO_2, further corroborating its improved catalytic activity.

4 Conclusions

In this study, Se-MnO_2 was engineered as an advanced catalyst for OER, achieving unprecedented activity and stability through dual electronic and structural modulation. The incorporation of Se atoms induces localized electron redistribution in MnO_2, stabilizing the catalytically active Mn^{3+} species while generating oxygen defect defects that synergistically regulate *OH adsorption energetics. *In situ* electrochemical Raman spectroscopy reveals that the Se dopants and oxygen defects collaboratively weaken the Mn–O bond strength, enabling dynamic reconstruction of active sites and suppressing excessive oxidation of Mn centers during OER. This electronic optimization allows the Se-MnO_2 catalyst to deliver current densities of 10 and 100 mA·cm^{-2} at remarkably low overpotentials of 345 ± 5 and 398 ± 5 mV in 0.5 M H_2SO_4, respectively. When integrated into PEM electrolyzers, the catalyst demonstrates exceptional durability over 400 h under dynamic current densities (100–500 mA·cm^{-2}), outperforming commercial RuO_2 and most non-precious metal-based counterparts. The work function alignment between Se-modified MnO_2 and reaction intermediates facilitates efficient charge transfer kinetics, balancing activity enhancement with corrosion resistance. This work establishes a paradigm for designing durable acidic OER catalysts through defect-dopant cooperativity, offering transformative potential for sustainable hydrogen production technologies.

Electronic Supplementary Material: Supplementary material (XRD patterns, XPS spectra, and LSV curves of different catalysts; ECSA test results; and Raman spectra) is available in the online version of this article at https://doi.org/10.26599/NR.2025.94907912.

Data availability

All data needed to support the conclusions in the paper are presented in the manuscript and the Electronic Supplementary Material. Additional data related to this paper may be requested from the corresponding author upon request.

Acknowledgements

The authors were supported by the National Natural Science Foundation of China (No. 52403363), the Hebei Natural Science Foundation (No. E2024203006), the Chunhui Program Cooperative Research Project of the Ministry of Education (No. 202200266), the Science Research Project of Hebei Education Department (No. BJ2025007), and the S&T Program of Qinhuangdao (No. 202401A131).

Declaration of competing interest

All the contributing authors report no conflict of interests in this work.

Author contribution statement

S. J. P. proposed the research and designed the experiments, wrote the manuscript, and directed the overall project. S. J. P. and S. A. W. carried out the experiments and performed *in situ* Raman characterizations. Z. S. X. conducted DFT calculations. Y. F. and H. L. helped with the analysis. D. S. W. oversaw the overall experimental process and reviewed the articles. All authors read and commented on the manuscript. All the authors have approved the final manuscript.

Use of AI statement

None.

References

[1] Ouimet, R. J.; Glenn, J. R.; De Porcellinis, D.; Motz, A. R.; Carmo, M.; Ayers, K. E. The role of electrocatalysts in the development of gigawatt-scale PEM electrolyzers. *ACS Catal.* **2022**, *12*, 6159–6171.

[2] Hubert, M. A.; King, L. A.; Jaramillo, T. F. Evaluating the case for reduced precious metal catalysts in proton exchange membrane electrolyzers. *ACS Energy Lett.* **2022**, *7*, 17–23.

[3] Kibsgaard, J.; Chorkendorff, I. Considerations for the scaling-up of water splitting catalysts. *Nat. Energy* **2019**, *4*, 430–433.

[4] Zhou, Z.; Su, Y. X.; Tan, H.; Wang, Y.; Huang, Q. W.; Wang, H. Z.; Wang, J. Y.; Kubo, M.; Ni, Z. T.; Kong, Y. et al. Atomically dispersed Co–P moieties via direct thermal exfoliation for alkaline hydrogen electrosynthesis. *J. Am. Chem. Soc.* **2025**, *147*, 3994–4004.

[5] Hao, Y. X.; Hung, S. F.; Wang, L. Q.; Deng, L. M.; Zeng, W. J.; Zhang, C. C.; Lin, Z. Y.; Kuo, C. H.; Wang, Y.; Zhang, Y. et al. Designing neighboring-site activation of single atom via tunnel ions for boosting acidic oxygen evolution. *Nat. Commun.* **2024**, *15*, 8015.

[6] Pei, Z. X.; Tan, H.; Gu, J. X.; Lu, L. G.; Zeng, X.; Zhang, T. Q.; Wang, C.; Ding, L. Y.; Cullen, P. J.; Chen, Z. F. et al. A polymeric hydrogel electrocatalyst for direct water oxidation. *Nat. Commun.* **2023**, *14*, 818.

[7] Shih, A. J.; Monteiro, M. C. O.; Dattila, F.; Pavesi, D.; Philips, M.; da Silva, A. H. M.; Vos, R. E.; Ojha, K.; Park, S.; van der Heijden, O. et al. Water electrolysis. *Nat. Rev. Methods Primers* **2022**, *2*, 84.

[8] An, L.; Wei, C.; Lu, M.; Liu, H. W.; Chen, Y. B.; Scherer, G. G.; Fisher, A. C.; Xi, P. X.; Xu, Z. J.; Yan, C. H. Recent development of oxygen evolution electrocatalysts in acidic environment. *Adv. Mater.* **2021**, *33*, 2006328.

[9] Zhao, T. T.; Shi, L.; Zhang, G. K.; Guo, Y. J.; Li, Y. Z.; Wang, J. Y.; Kong, S. Y.; Zheng, Q.; Yang, Y. R.; Tan, T. et al. Compressive strain in high-entropy alloy for high-performance acidic oxygen evolution. *Matter* **2025**, *8*, 102091.

[10] Zaman, S.; Khalid, M.; Shahgaldi, S. Advanced electrocatalyst supports for proton exchange membrane water electrolyzers. *ACS Energy Lett.* **2024**, *9*, 2922–2935.

[11] Zhang, B.; Zheng, X. L.; Voznyy, O.; Comin, R.; Bajdich, M.; García-Melchor, M.; Han, L. L.; Xu, J. X.; Liu, M.; Zheng, L. R. et al. Homogeneously dispersed multimetal oxygen-evolving catalysts. *Science* **2016**, *352*, 333–337.

[12] Yan, D. F.; Li, Y. X.; Huo, J.; Chen, R.; Dai, L. M.; Wang, S. Y. Defect chemistry of nonprecious-metal electrocatalysts for oxygen reactions. *Adv. Mater.* **2017**, *29*, 1606459.
[13] Elmaalouf, M.; Odziomek, M.; Duran, S.; Gayrard, M.; Bahri, M.; Tard, C.; Zitolo, A.; Lassalle-Kaiser, B.; Piquemal, J. Y.; Ersen, O. et al. The origin of the high electrochemical activity of pseudo-amorphous iridium oxides. *Nat. Commun.* **2021**, *12*, 3935.
[14] Kasian, O.; Grote, J. P.; Geiger, S.; Cherevko, S.; Mayrhofer, K. J. J. The common intermediates of oxygen evolution and dissolution reactions during water electrolysis on iridium. *Angew. Chem., Int. Ed.* **2018**, *57*, 2488–2491.
[15] Chen, F. Y.; Qiu, C.; Wu, Z. Y.; Wi, T. U.; Finfrock, Y. Z.; Wang, H. T. Ruthenium-lead oxide for acidic oxygen evolution reaction in proton exchange membrane water electrolysis. *Nano Res.* **2024**, *17*, 8671–8677.
[16] Zhao, S.; Hung, S. F.; Deng, L. M.; Zeng, W. J.; Xiao, T.; Li, S. X.; Kuo, C. H.; Chen, H. Y.; Hu, F.; Peng, S. J. Constructing regulable supports via non-stoichiometric engineering to stabilize ruthenium nanoparticles for enhanced pH-universal water splitting. *Nat. Commun.* **2024**, *15*, 2728.
[17] Shi, Z. P.; Li, J.; Wang, Y. B.; Liu, S. W.; Zhu, J. B.; Yang, J. H.; Wang, X.; Ni, J.; Jiang, Z.; Zhang, L. J. et al. Customized reaction route for ruthenium oxide towards stabilized water oxidation in high-performance PEM electrolyzers. *Nat. Commun.* **2023**, *14*, 843.
[18] Pan, S. J.; Li, H.; Liu, D.; Huang, R.; Pan, X. L.; Ren, D.; Li, J.; Shakouri, M.; Zhang, Q. X.; Wang, M. J. et al. Efficient and stable noble-metal-free catalyst for acidic water oxidation. *Nat. Commun.* **2022**, *13*, 2294.
[19] Park, J.; Liu, E.; Angizi, S.; Abdellah, A.; Kirici, E. Y.; Higgins, D. Formation of core–shell Ir@TiO_2 nanoparticles through hydrogen treatment as acidic oxygen evolution reaction catalysts. *Adv. Funct. Mater.* **2024**, *34*, 2408848.
[20] Pan, S. J.; Li, H.; Wang, T. Y.; Fu, Y.; Wang, S. N.; Xie, Z. S.; Wei, L.; Li, H.; Li, N. Er-doping enhances the oxygen evolution performance of cobalt oxide in acidic medium. *ACS Catal.* **2024**, *14*, 13814–13824.
[21] Chen, X.; Xu, X. Y.; Shao, C. P.; Ke, Z. Y.; Cheng, Y. W.; Jin, H. Q.; Da, Y. M.; Liu, D. M.; Chen, W. Facet-dependent lattice oxygen activation on oxygen-defective Co_3O_4 for electrocatalytic oxygen evolution reaction. *ACS Energy Lett.* **2024**, *9*, 2182–2192.
[22] Post, J. E. Manganese oxide minerals: Crystal structures and economic and environmental significance. *Proc. Natl. Acad. Sci. USA* **1999**, *96*, 3447–3454.
[23] Umena, Y.; Kawakami, K.; Shen, J. R.; Kamiya, N. Crystal structure of oxygen-evolving photosystem II at a resolution of 1.9 Å. *Nature* **2011**, *473*, 55–60.
[24] Huynh, M.; Bediako, D. K.; Nocera, D. G. A functionally stable manganese oxide oxygen evolution catalyst in acid. *J. Am. Chem. Soc.* **2014**, *136*, 6002–6010.
[25] Takashima, T.; Hashimoto, K.; Nakamura, R. Mechanisms of pH-dependent activity for water oxidation to molecular oxygen by MnO_2 electrocatalysts. *J. Am. Chem. Soc.* **2012**, *134*, 1519–1527.
[26] Huynh, M.; Shi, C. Y.; Billinge, S. J. L.; Nocera, D. G. Nature of activated manganese oxide for oxygen evolution. *J. Am. Chem. Soc.* **2015**, *137*, 14887–14904.
[27] Morgan Chan, Z.; Kitchaev, D. A.; Nelson Weker, J.; Schnedermann, C.; Lim, K.; Ceder, G.; Tumas, W.; Toney, M. F.; Nocera, D. G. Electrochemical trapping of metastable Mn^{3+} ions for activation of MnO_2 oxygen evolution catalysts. *Proc. Natl. Acad. Sci. USA* **2018**, *115*, E5261–E5268.
[28] Jin, H. Y.; Liu, X. Y.; An, P. F.; Tang, C.; Yu, H. M.; Zhang, Q. H.; Peng, H. J.; Gu, L.; Zheng, Y.; Song, T. et al. Dynamic rhenium dopant boosts ruthenium oxide for durable oxygen evolution. *Nat. Commun.* **2023**, *14*, 354.
[29] Wang, Y.; Yang, R.; Ding, Y. J.; Zhang, B.; Li, H.; Bai, B.; Li, M. R.; Cui, Y.; Xiao, J. P.; Wu, Z. S. Unraveling oxygen vacancy site mechanism of Rh-doped RuO_2 catalyst for long-lasting acidic water oxidation. *Nat. Commun.* **2023**, *14*, 1412.
[30] Liu, H.; Zhang, Z.; Fang, J. J.; Li, M. X.; Sendeku, M. G.; Wang, X.; Wu, H. Y.; Li, Y. P.; Ge, J. J.; Zhuang, Z. B. et al. Eliminating over-oxidation of ruthenium oxides by niobium for highly stable electrocatalytic oxygen evolution in acidic media. *Joule* **2023**, *7*, 558–573.
[31] Wen, Y. Z.; Chen, P. N.; Wang, L.; Li, S. Y.; Wang, Z. Y.; Abed, J.; Mao, X. N.; Min, Y. M.; Dinh, C. T.; Luna, P. D. et al. Stabilizing highly active Ru sites by suppressing lattice oxygen participation in acidic water oxidation. *J. Am. Chem. Soc.* **2021**, *143*, 6482–6490.
[32] Pan, S. J.; Xie, Z. S.; Li, H.; Wang, S. N.; Fu, Y.; Wang, D. S. The acceleration of the active phase transition of NiCoFe hydroxide by Ta doping to achieve long-time seawater electrolysis at Ampere-level current density. *Fuel* **2024**, *369*, 131802.
[33] Ma, K. X.; Ge, S. Y.; Fu, R. R.; Feng, C. H.; Zhao, H. Y.; Shen, X. R.; Liang, G. F.; Zhao, Y.; Jiao, Q. Z. Uncovering Se, P co-doping effect in MnO_2 toward high-performance aqueous zinc-ion batteries. *Chem. Eng. J.* **2024**, *484*, 149525.
[34] Jiang, Y. W.; Gao, S. S.; Liu, X. J.; Wang, Y.; Zhou, S. X.; Liu, Q.; Abdukayum, A.; Hu, G. Z. Recent achievements in selenium-based transition metal electrocatalysts for pH-universal water splitting. *Nano Res.* **2024**, *17*, 5763–5785.
[35] Gorlin, Y.; Lassalle-Kaiser, B.; Benck, J. D.; Gul, S.; Webb, S. M.; Yachandra, V. K.; Yano, J.; Jaramillo, T. F. *In situ* X-ray absorption spectroscopy investigation of a bifunctional manganese oxide catalyst with high activity for electrochemical water oxidation and oxygen reduction. *J. Am. Chem. Soc.* **2013**, *135*, 8525–8534.
[36] Menezes, P. W.; Walter, C.; Hausmann, J. N.; Beltrán-Suito, R.; Schlesiger, C.; Praetz, S.; Yu Verchenko, V.; Shevelkov, A. V.; Driess, M. Boosting water oxidation through *in situ* electroconversion of manganese gallide: An intermetallic precursor approach. *Angew. Chem., Int. Ed.* **2019**, *58*, 16569–16574.
[37] Tran, G. S.; Vo, T. G.; Chiang, C. Y. *Operando* revealing the crystal phase transformation and electrocatalytic activity correlation of MnO_2 toward glycerol electrooxidation. *ACS Appl. Mater. Interfaces* **2023**, *15*, 22662–22671.
[38] Chen, D. C.; Ding, D.; Li, X. X.; Waller, G. H.; Xiong, X. H.; El-Sayed, M. A.; Liu, M. L. Probing the charge storage mechanism of a pseudocapacitive MnO_2 electrode using in *operando* Raman spectroscopy. *Chem. Mater.* **2015**, *27*, 6608–6619.